



HAL
open science

Broadening and Redward Asymmetry of $H\alpha$ Line Profiles Observed by LAMOST during a Stellar Flare on an M-type Star

Yuchuan Wu, Hechao Chen, Hui Tian, Liyun Zhang, Jianrong Shi, Han He,
Hongpeng Lu, Yu Xu, Haifeng Wang

► **To cite this version:**

Yuchuan Wu, Hechao Chen, Hui Tian, Liyun Zhang, Jianrong Shi, et al.. Broadening and Redward Asymmetry of $H\alpha$ Line Profiles Observed by LAMOST during a Stellar Flare on an M-type Star. The Astrophysical Journal, 2022, 928, 10.3847/1538-4357/ac5897 . insu-03719736

HAL Id: insu-03719736

<https://insu.hal.science/insu-03719736>

Submitted on 11 Jul 2022

HAL is a multi-disciplinary open access archive for the deposit and dissemination of scientific research documents, whether they are published or not. The documents may come from teaching and research institutions in France or abroad, or from public or private research centers.

L'archive ouverte pluridisciplinaire **HAL**, est destinée au dépôt et à la diffusion de documents scientifiques de niveau recherche, publiés ou non, émanant des établissements d'enseignement et de recherche français ou étrangers, des laboratoires publics ou privés.



Distributed under a Creative Commons Attribution 4.0 International License



Broadening and Redward Asymmetry of H α Line Profiles Observed by LAMOST during a Stellar Flare on an M-type Star

Yuchuan Wu¹, Hechao Chen¹ , Hui Tian^{1,2} , Liyun Zhang^{3,4}, Jianrong Shi² , Han He^{5,6} , Hongpeng Lu¹ , Yu Xu¹, and Haifeng Wang⁷

¹ School of Earth and Space Sciences, Peking University, Beijing 100871, People's Republic of China; hechao.chen@pku.edu.cn, huitian@pku.edu.cn

² National Astronomical Observatories, Chinese Academy of Sciences, Beijing 100101, People's Republic of China

³ College of Physics, Guizhou University, Guiyang 550025, People's Republic of China

⁴ Key Laboratory for the Structure and Evolution of Celestial Objects, Chinese Academy of Sciences, Kunming 650011, People's Republic of China

⁵ CAS Key Laboratory of Solar Activity, National Astronomical Observatories, Chinese Academy of Sciences, Beijing 100101, People's Republic of China

⁶ University of Chinese Academy of Sciences, Beijing 100049, People's Republic of China

⁷ GEPI, Observatoire de Paris, Université PSL, CNRS, Place Jules Janssen F-92195, Meudon, France

Received 2021 December 12; revised 2022 February 22; accepted 2022 February 23; published 2022 April 7

Abstract

Stellar flares are characterized by sudden enhancement of electromagnetic radiation in stellar atmospheres. So far, much of our understanding of stellar flares has come from photometric observations, from which plasma motions in flare regions could not be detected. From the spectroscopic data of LAMOST DR7, we have found one stellar flare that is characterized by an impulsive increase followed by a gradual decrease in the H α line intensity on an M4-type star, and the total energy radiated through H α is estimated to be of the order of 10^{33} erg. The H α line appears to have a Voigt profile during the flare, which is likely caused by Stark pressure broadening due to the dramatic increase in electron density and/or opacity broadening due to the occurrence of strong nonthermal heating. Obvious enhancement has been identified in the red wing of the H α line profile after the impulsive increase in the H α line intensity. The red-wing enhancement corresponds to plasma moving away from the Earth at a velocity of 100–200 km s⁻¹. According to our current knowledge of solar flares, this red-wing enhancement may originate from: (1) flare-driven coronal rain, (2) chromospheric condensation, or (3) a filament/prominence eruption either with nonradial backward propagation or with strong magnetic suppression. The total mass of the moving plasma is estimated to be of the order of 10^{15} kg.

Unified Astronomy Thesaurus concepts: [Stellar flares \(1603\)](#); [Stellar coronal mass ejections \(1881\)](#); [Late-type dwarf stars \(906\)](#); [Time domain astronomy \(2109\)](#); [Spectroscopy \(1558\)](#)

1. Introduction

Stellar flares are dramatic explosions in stellar atmospheres, which are often characterized by a rapid rise followed by a slow decrease in the electromagnetic radiation across a wide range of wavelength from radio to γ -rays. On late-type main-sequence stars, these flare events are generally thought to be triggered by a sudden release of magnetic energy in magnetized stellar atmospheres (Haisch et al. 1991). According to the widely accepted solar flare scenario (e.g., Benz and Güdel 2010; Shibata & Magara 2011), magnetic reconnection and its associated rapid energy release in the corona play a key role in triggering solar flares. During this process an enormous amount of energy is transported to the lower solar atmosphere and dissipates in the dense chromosphere via thermal conduction and thermalization of (relativistic) energetic electrons. This leads to intense localized plasma heating, which in turn results in chromospheric evaporation and condensation mainly in the impulsive phase of flares (e.g., Fletcher et al. 2011). In the meantime, a continuous increase in the local temperature, electron density, and plasma velocity would cause strong enhancement and broadening of chromospheric spectral lines such as the H α line. Hence, spectroscopic observations of chromospheric lines have long been important

diagnostics for the physical processes behind solar and stellar flares.

After decades of multiwavelength imaging observations of solar flares, solar physicists have learned that a solar flare is only part of a large-scale process of eruptive energy release, in which the flare occurs low in the atmosphere and a coronal mass ejection (CME) may take place on a much larger scale (e.g., Lin et al. 2003; Zhang & Low 2005; Chen 2011; Shibata & Magara 2011; Osten & Wolk 2017). In fact, CMEs play the most important role in driving hazardous space weather in the near-Earth space environment (Gosling 1993). Statistically, flares and CMEs on the Sun are more closely associated with each other with increasing flare class (e.g., Yashiro & Gopalswamy 2009; Aarnio et al. 2011). Recent photometric observations from the Kepler spacecraft and the Transiting Exoplanet Survey Satellite revealed a lot of superflares on G-, K-, and M-type stars (e.g., Maehara et al. 2012; Notsu et al. 2013; He et al. 2015, 2018; Namekata et al. 2017; Doyle et al. 2020; Tu et al. 2020, 2021; Yan et al. 2021). The total energy released by one such superflare (10^{33} – 10^{38} erg) often far exceeds that of the strongest solar flare (with energy up to 10^{32} erg) (Schaefer et al. 2000; Shibata et al. 2013), indicating that they are possibly associated with monster CMEs. Studying stellar flares and associated CMEs of these late-type stars, especially active M dwarfs, is of particular interest. This is because most known potentially habitable exoplanets are orbiting around such stars (Alvarado-Gómez et al. 2021). If frequent high-energy flares and associated CMEs take place on



Original content from this work may be used under the terms of the [Creative Commons Attribution 4.0 licence](#). Any further distribution of this work must maintain attribution to the author(s) and the title of the work, journal citation and DOI.

these stars, they may impact or even threaten the habitability of nearby exoplanets (Khodachenko et al. 2007; Yelle et al. 2008). However, detection of CMEs on these stars is still challenging, since direct imaging of stellar coronae is almost impossible even for the nearest stars (see a brief review by Moschou et al. 2019).

On the Sun, flare processes can be spatially resolved in great detail. As a result, characteristics of the line broadening and asymmetry during different phases of solar flares have been well studied through many observations (e.g., Švestka 1972; Schmieder et al. 1987; Zarro et al. 1988). For instance, a symmetric chromospheric line broadening is often believed to be caused by the Stark effect or turbulence (e.g., Kowalski et al. 2017; Zhu et al. 2019), while an asymmetric line broadening is usually explained by bulk plasma motion in the form of chromospheric evaporation (e.g., Canfield et al. 1990; Li & Ding 2011; Li et al. 2022), chromospheric condensation (e.g., Ichimoto & Kurokawa 1984; Fisher et al. 1985; Gan et al. 1993; Ding et al. 1995; Tian et al. 2015; Zhang et al. 2016; Tei et al. 2018; Yu et al. 2020), or coronal rain (e.g., Antolin 2020; Li et al. 2020a; Chen et al. 2022; Schad et al. 2021).

As an extension of solar spectroscopic studies, spectroscopic observations of chromospheric lines on other stars have been used not only to understand the dynamics of stellar flares, but also to detect flare-associated CMEs, since CMEs generally host a dense core at chromospheric temperature, i.e., the erupting cool prominence/filament (e.g., Illing & Hundhausen 1985). For instance, Houdebine et al. (1990) found an obvious enhancement in the blue wings of Balmer lines during a flare occurring on the well-known flaring dMe dwarf, AD Leo. The blueward asymmetry corresponds to a high speed of 5800 km s^{-1} , which has been explained as a possible CME. With spectroscopic observations, Crespo-Chacón et al. (2006) conducted a systematic flare study on AD Leo, in which the three strongest ones are found to be associated with Balmer line broadening and two show weak redward asymmetries. Vida et al. (2016) reported a complex CME with material falling back and re-ejected on the M4 dwarf V374 Peg, in which its associated blueshift (675 km s^{-1}) is above the stellar surface escape velocity ($\sim 580 \text{ km s}^{-1}$). From high-resolution spectra of 28 active M dwarfs, Fuhrmeister et al. (2018) identified broad, potentially asymmetric, wings in $H\alpha$ during stellar flares. They explained the observed red asymmetries as a process similar to chromospheric downward condensation or coronal rain, and suggested that the line broadening may be caused by the Stark effect. Recently, several authors have tried to search for CMEs on some flaring M dwarfs with time-resolved spectra (Muheki et al. 2020; Maehara et al. 2021). Two candidates for erupting filaments/prominences have been reported, on EV Lac and YZ CMi. With photometric and follow-up spectroscopic observations, Wang et al. (2021) reported the detection of possible CMEs during flares of two M dwarfs. In addition, focusing on more than 5500 spectra of M-dwarf stars, Vida et al. (2019) found 478 spectra with Balmer line asymmetries, most of which are associated with flux enhancement, and their maximum velocities are of the order of $100\text{--}300 \text{ km s}^{-1}$. Similarly, Muheki et al. (2020) and Koller et al. (2021) respectively used a large number of spectra to search for flares and CMEs on M dwarfs, but consistently reported a high level of flare activity and a low detection rate of CME candidates. More recently, Namekata et al. (2022) successfully detected definite evidence of a flare–filament eruption event on the G-type star EK Draconis using time-

resolved $H\alpha$ spectroscopic observations; moreover, they compared this signature of stellar eruption with solar filament eruptions in the Sun-as-a-star spectral view, revealing that the former is the same as a magnified version of the latter.

From the spectra provided by the Large Sky Area Multi-Object Fiber Spectroscopic Telescope (LAMOST), we have found one interesting stellar flare with obviously broadened and asymmetric $H\alpha$ line profiles. In Section 2, we describe the observational data and show results of analysis of the event, including the Voigt–Gauss function fitting and red–blue asymmetry analysis. In Section 3, we estimate the flare energy and mass of the moving plasma, and provide explanations for the Lorentz profile and asymmetry of $H\alpha$. Finally, conclusions are given in Section 4.

2. Observation and Results of Data Analysis

LAMOST, also called the Guoshoujing Telescope, is a medium-aperture (4.6 m) optical telescope in China, with the capability of performing spectral surveys of the northern-sky stars in the Milky Way and other objects (Su et al. 1998; Cui et al. 2012). In recent years, LAMOST has provided spectra in the time domain, making it possible to search for stellar flares through the time evolution of $H\alpha$ line intensity and profile asymmetry. Here we used data from LAMOST DR7 to search for $H\alpha$ line asymmetries. In the LAMOST DR7 medium-resolution ($R \sim 7500$) spectral catalog, there are 2,828,655 time-domain spectra, covering the wavelength range $6300\text{--}6800 \text{ \AA}$. These spectra were taken between 2017 September 28 and 2019 June 8.

The stellar flare we study here was observed on 2019 January 16, and the starting observation time is 23:37 (local time), or 15:37 (UT). The obsid is 716907097. The original time-domain spectra of the $H\alpha$, He I 6680 \AA , and Mg I 5171 \AA lines are shown in Figure 1. Each exposure lasts for 20 minutes, and the time cadence of exposures is around 23 minutes. From Figure 1, we can see that obvious radiation enhancement and profile broadening of the $H\alpha$ line commence at 70 minutes after the starting time and last to the end of this observation. Other chromospheric lines like He I and Mg I become visible during the flare, and their intensities decrease in the later phase of the flare. Interestingly, a red-wing enhancement of the $H\alpha$ line was also presented in the later phase of the flare, indicating the presence of materials (plasma) moving away from the Earth. To get a clearer view of the red-wing enhancement, see Figure 2 in Section 2.1. LAMOST provides signal-to-noise ratios (S/Ns) that were calculated from the formula $\text{flux} \times (\text{inverse variance})^{0.5}$. The eight spectra of the star have S/Ns of 10.02, 9.96, 10.13, 27.04, 23.64, 13.27, 11.62, and 10.13. Note that after taking the Earth’s motion and the star’s redshift into consideration, the corrected theoretical line center of the $H\alpha$ profile is 6564.61 \AA .

According to the LAMOST catalog⁸, this target is an M4-type star, and other relevant data are shown in Table 1. The star was also observed during Kepler’s second mission (Howell et al. 2014), and several flares were detected on it.⁹ We used the effective temperature to estimate the mass and radius of the star. We can find the average radius, mass, and effective

⁸ <http://dr7.lamost.org/v2.0/spectrum/view?obsid=432616084>

⁹ The K2 observations of this star can be found from <https://mast.stsci.edu/portal/Mashup/Clients/Mast/Portal.html> or <https://drive.google.com/drive/folders/1K46MbuEarPNwNwRlR0n8dR7eCpPkYzDy?usp=sharing>.

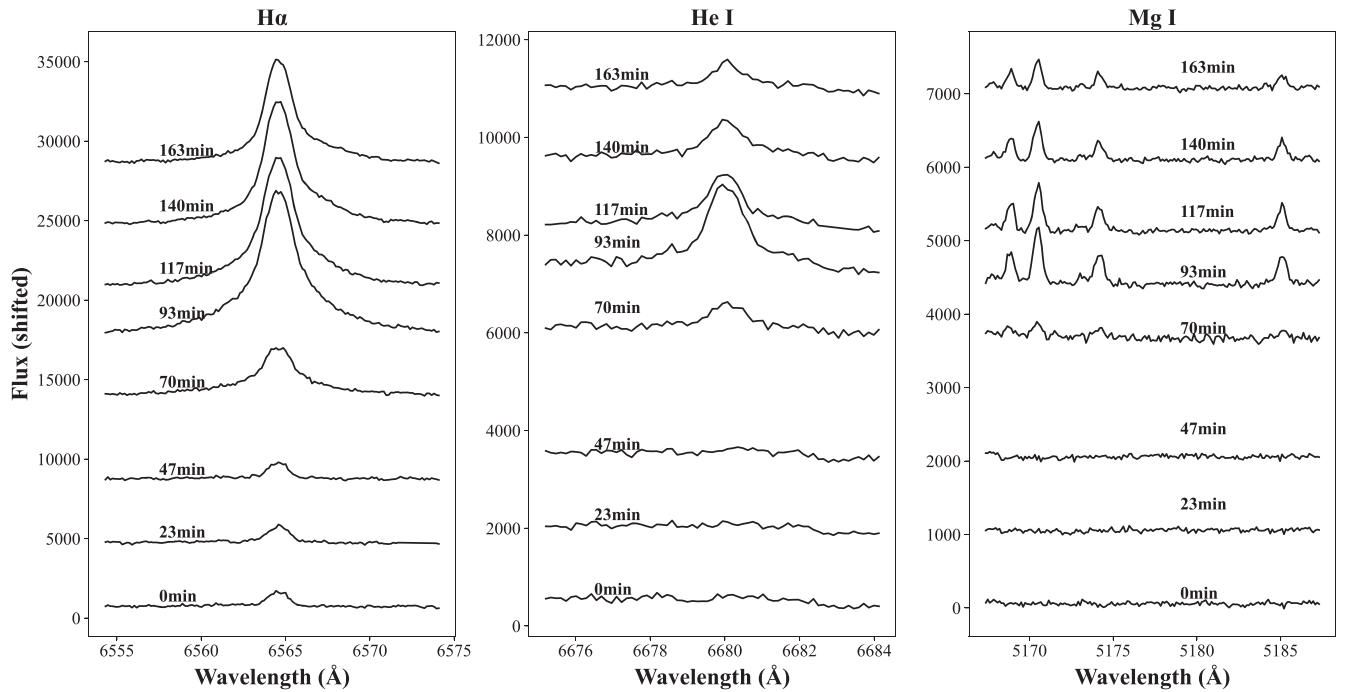


Figure 1. $H\alpha$, He I, and Mg I line profiles observed at different times during the flare of interest. The profiles are shifted on the y-axis for a better illustration.

temperature of an M2- or M5-type main-sequence star from Cox & Pilachowski (2000). We then assumed a linear relationship of $\lg(M/M_{\odot})$ and $\lg(R/R_{\odot})$ versus $\lg T_{\text{eff}}$ for stars with a spectral type between M2 and M5. Here M , M_{\odot} , R , and R_{\odot} represent the masses and radii of the star and our Sun, respectively, and T_{eff} is the effective temperature of a star. Since the effective temperature of the observed star is 3404 K, we obtained the following:

$$\frac{M}{M_{\odot}} = 0.326, \quad \frac{R}{R_{\odot}} = 0.411. \quad (1)$$

Then we can calculate the escape velocity of the star, which is 550 km s^{-1} .

2.1. Normalized Spectra

The continuum levels of the original $H\alpha$ spectra vary with time, e.g., in the fourth and fifth exposures the continuum levels are about twice as large as in other exposures. This variation is too big to be explained by a white-light flare. Instead, it is more likely caused a variation in seeing. Due to the lack of absolute flux calibration, we thus assumed that the continuum level remains unchanged before, during, and after the flare. However, we also point out that the $H\alpha$ flare might be associated with a white-light flare, especially considering that the broadened $H\alpha$ profiles observed in the flare (see Figure 2) indicate a nonthermal heating process (see details in Section 3.3 and also Namekata et al. 2020), but we cannot confirm whether a white-light flare exists from the available data. Before further analysis, we need to normalize the original spectra to the continuum intensities. To obtain the continuum intensities, we used a summation of a Voigt function, a Gauss function (only for the last four spectra), and a constant background to fit each $H\alpha$ profile. The constant was taken as the continuum level. The Gauss function was

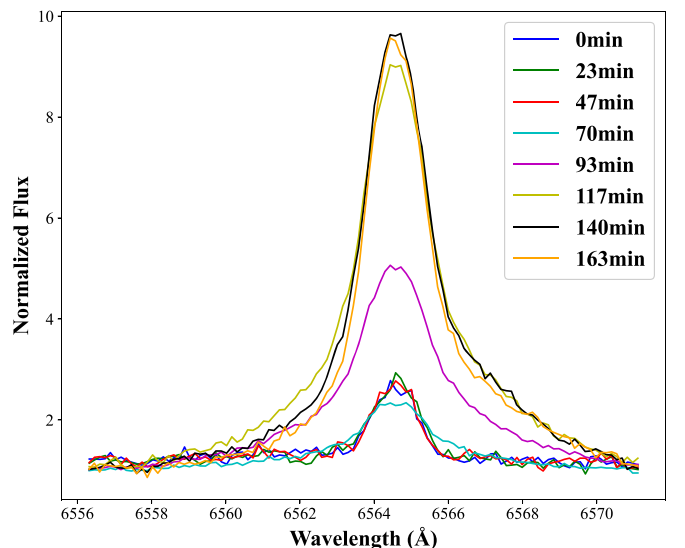


Figure 2. $H\alpha$ line profiles normalized to the continuum intensities.

introduced here to account for the additional bulk flow component, which can be inferred from the redward asymmetry. The Voigt function is a convolution of a Lorentz function and a Gauss function. A Voigt function fitting has often been applied to analyze the spectral broadening of hydrogen Balmer lines (i.e., $H\alpha$, $H\beta$) (e.g., Luque et al. 2003; Tremblay & Bergeron 2009; Falcon et al. 2015) and helium lines (e.g., Kanodia et al. 2022; Schad et al. 2021) in astrophysical and laboratory plasmas. Here, we used it to fit the $H\alpha$ line profile because the chromospheric line broadening is likely dominated by a combination of pressure broadening and Doppler broadening during flares, which can be described as a Voigt function

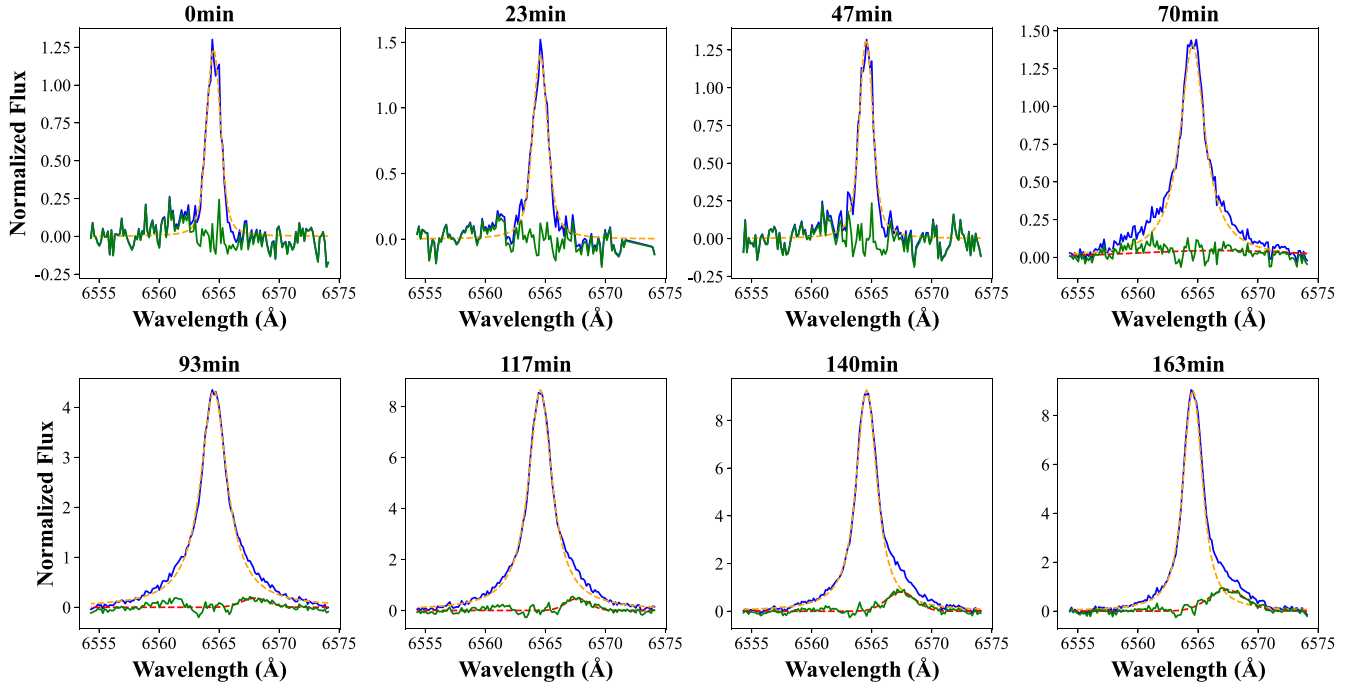


Figure 3. Normalized H α line profiles and their fitting results. Blue lines are the original data, orange lines are fitting results for Voigt function, red lines are fitting results for Gauss function, and green lines indicate residuals between fitting results for Voigt function and observation.

Table 1
Basic Information on the Star (716907097)

R.A. (deg)	Decl. (deg)	Subclass	Redshift	Effective Temperature (K)	Surface Gravity, $\log g$ (cm s^{-2})	Magnitudes of g Filter	Magnitudes of r Filter	Magnitudes of i Filter
127.52	16.57	dM4	0.00012	3404	5.02	15.82	14.53	13.04

(Zhu et al. 2019). The total fitting function can be written as follows (Ginsburg & Mirocha 2011):

$$I(\lambda) = \frac{\text{Re} \left[\text{wofz} \left(\frac{\lambda - \lambda_{\text{cen}} + i\gamma}{\sqrt{2}\sigma} \right) \right]}{\sqrt{2\pi}\sigma} I_0 + a e^{-\left(\frac{\lambda-m}{s}\right)^2} + C, \quad (2)$$

where λ and λ_{cen} are the wavelength and centroid wavelength of the H α line, respectively. Re represents the real part of a complex number. And wofz is the Faddeeva function, which satisfies $\text{wofz}(z) = e^{-z^2} \text{erfc}(-iz)$.

There are seven free parameters: I_0 characterizes the total flux of the Voigt function; γ is the half width at half maximum (HWHM) of the Lorentzian component. A larger γ means that the Voigt function is more similar to a Lorentz profile, indicating a larger effect of pressure broadening. The parameter σ is the standard deviation of the Gaussian component in the Voigt function. The height, centroid, and width of the Gauss function are represented by a , m , and s , respectively. The continuum level is represented by C . By dividing the original spectrum taken during each exposure by C , we obtained the normalized spectrum $I_n(\lambda)$. All normalized spectra are shown in Figure 2.

2.2. Voigt–Gauss Function Fitting

We used the same function to fit the normalized spectra. After normalization, the fitting function becomes

$$I_n(\lambda) = \frac{\text{Re} \left[\text{wofz} \left(\frac{\lambda - \lambda_{\text{cen}} + i\gamma}{\sqrt{2}\sigma} \right) \right]}{\sqrt{2\pi}\sigma} I_{n,0} + a_n e^{-\left(\frac{\lambda-m}{s}\right)^2} + 1. \quad (3)$$

The subscript n means normalized intensity. The normalized spectrum, fitting function, and the residual between fitting and observation for each exposure are shown in Figure 3. Note that we removed the continuum just for the sake of simplicity. The variations of I_0 , widths of the Gaussian and Lorentzian components of the Voigt–Gaussian fitting function, as well as the fitting parameters of the Gaussian function are shown in Figure 4.

From Figures 3 and 4, we noticed the following characteristics:

1. The total flux of the Voigt function, I_0 , increases quickly between 70 and 117 minutes, indicating the occurrence of a flare.
2. The HWHM of the Gaussian component in the Voigt–Gauss fitting function is close to 0 for three spectra taken at 70, 93, and 117 minutes. At these occasions, the wings of the H α line profiles are clearly characterized as a Lorentz

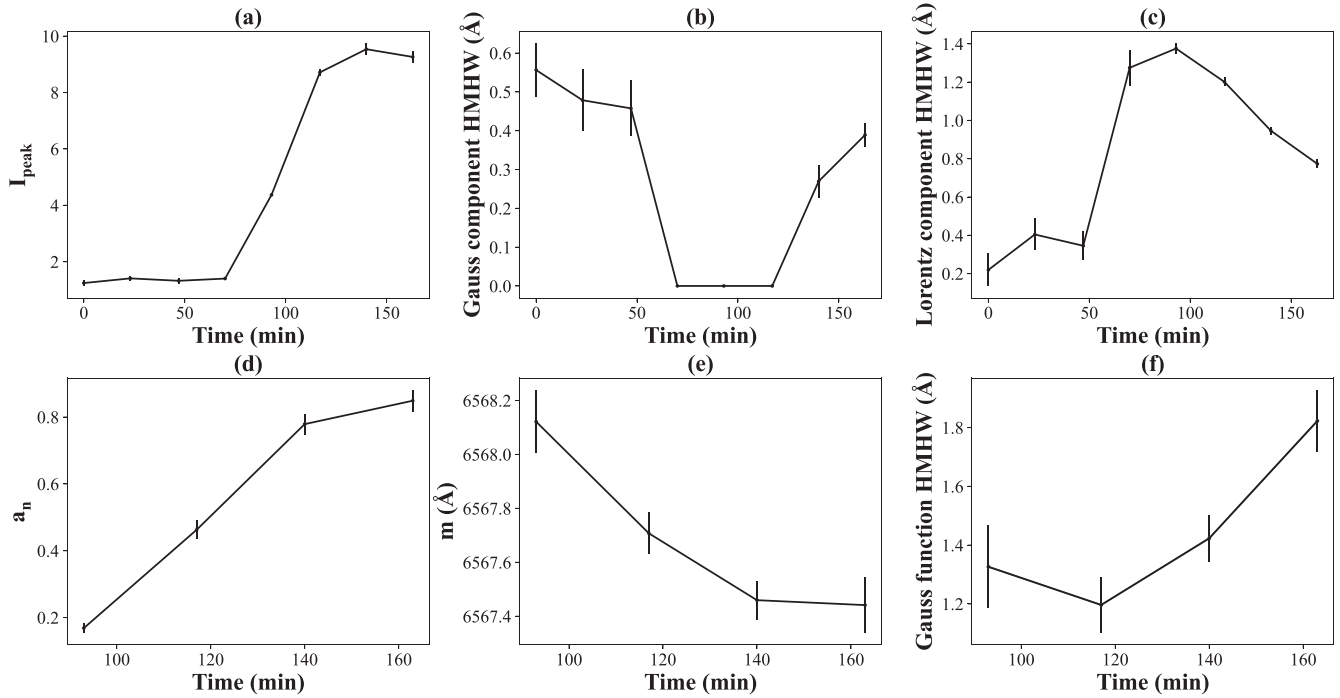


Figure 4. Time evolution of the fitting parameters. The top rows show the total flux of the Voigt function (I_0), the HWHM of the Gaussian component ($\sigma\sqrt{\ln 4}$), and the HWHM of the Lorentzian component (γ) in the Voigt–Gauss function, respectively. The bottom row only shows the height (a_n), the centroid (m), and the HWHM ($s\sqrt{\ln 2}$) in the Gaussian function for the last four spectra, where profile asymmetries are observed. In each panel, the error bars represent uncertainties calculated from the fitting errors.

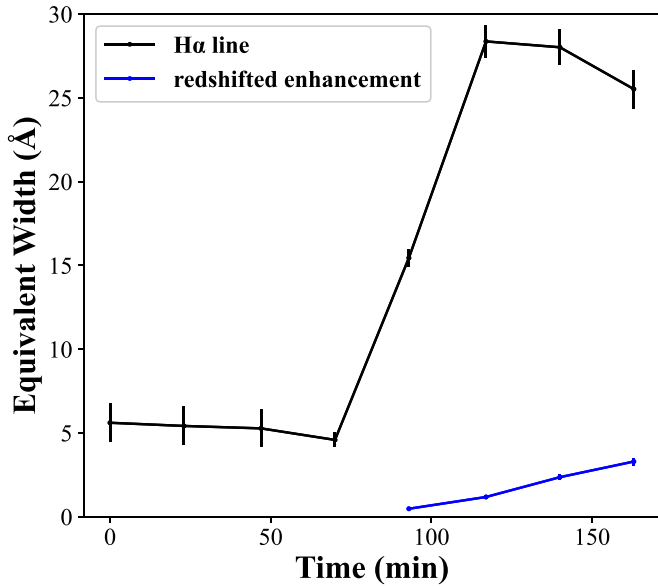


Figure 5. Time variations of the equivalent widths of the $H\alpha$ line and the redshifted enhancement. The black error bars indicate uncertainties of the equivalent width of the $H\alpha$ line by summing the measurement errors between 6557 and 6572 \AA . The blue error bars represent the uncertainties of the equivalent width of the redshifted enhancement as calculated from the fitting errors.

function. Interestingly, this change of spectral profile starts as soon as the rapid increase in I_0 . When the rapid increase in I_0 stops, the HWHM of the Gaussian component in the Voigt–Gauss fitting function begins to increase.

3. a_n keeps on increasing after 93 minutes, meaning that the redward asymmetry of the $H\alpha$ line profile becomes more and more significant.

4. m slowly decreases after 93 minutes, indicating that the moving plasma responsible for the redward asymmetry of $H\alpha$ possibly decelerates after 93 minutes (see Figure 4). From 93 minutes to 163 minutes, the average deceleration rate was estimated as 7.6 m s^{-2} .

The time variation of the integrated $H\alpha$ flux can reflect the change in radiation power through the $H\alpha$ line. We first integrated each normalized spectrum from 6557 to 6572 \AA , then removed the continuum. The remaining integral is the equivalent width of the $H\alpha$ line. Using the fitting parameters of the Gauss function, we can also obtain the equivalent width of the redshifted enhancement responsible for the line asymmetry in the last four exposures. The time variations of the equivalent widths of the $H\alpha$ line and the redshifted enhancement are shown in Figure 5. We can see that the equivalent width of the $H\alpha$ line increases quickly between 70 and 117 minutes, and decreases slowly after 117 minutes, which validates the conclusion from the analysis of the total flux of the Voigt function. At the same time, the equivalent width of the redshifted enhancement simultaneously grows by a factor of ~ 6 from 93 to 163 minutes.

2.3. Red–Blue Asymmetry Analysis

A technique called red–blue (RB) asymmetry analysis has been often used to analyze the asymmetries of solar spectral lines both under the quiet-Sun condition (e.g., De Pontieu et al. 2009; Tian et al. 2011) and during solar eruptions (Tian et al. 2012). The technique can reveal where the asymmetry is most obvious. Here we used this method to analyze the asymmetry of the $H\alpha$ line profiles. The RB asymmetry for an offset

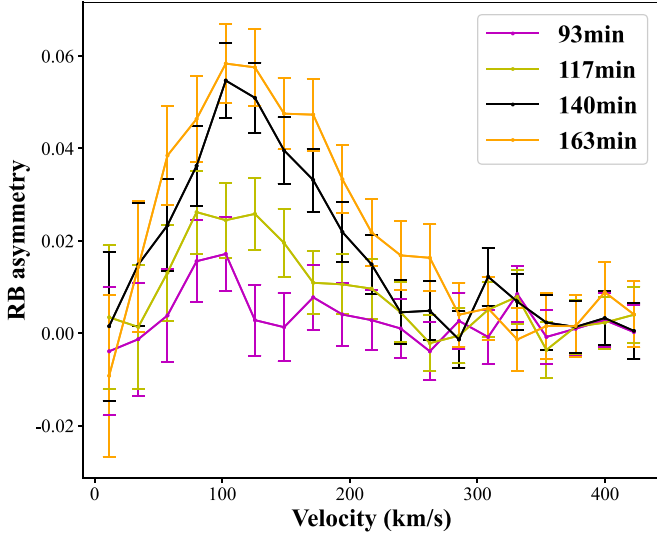


Figure 6. Results of RB asymmetry analysis for the $H\alpha$ spectral profiles taken during the last four exposures. The error bars indicate the uncertainties propagated from the measurement errors.

velocity can be expressed as

$$RB(u_c) = \int_{u_c - \delta u/2}^{u_c + \delta u/2} I(u) du - \int_{-u_c - \delta u/2}^{-u_c + \delta u/2} I(u) du, \quad (4)$$

where u_c , δu , and $I(u)$ respectively represent the velocity from the line center, the velocity range over which the RB asymmetry is determined, and the ratio between spectral intensity and peak intensity. Here the $H\alpha$ line center and peak intensity are λ_{cen} and I_0 , respectively, as calculated in Section 2.1. We found that a smaller δu leads to too much fluctuation, and a bigger δu ignores too much data in the spectra. By trial and error, we found that 0.5 \AA is just appropriate for our calculation. So we let δu be the velocity corresponding to a Doppler shift of 0.5 \AA , which is around 22.8 km s^{-1} . We calculated RB as a function of u_c , where $u_c = 22.8 \times (0.5 + n) \text{ km s}^{-1}$, $n = 0, 1, 2, \dots$.

The results of the RB asymmetry analysis for the spectra taken during the last four exposures are shown in Figure 6. We can see that an obvious redward asymmetry, which is indicated by the positive peak of an RB asymmetry profile, is clearly present after 93 minutes, when the $H\alpha$ line intensity shows an impulsive increase. The redward asymmetry becomes more evident toward the end of the observation. The peaks of the RB asymmetry profiles indicate a redshifted velocity of $100\text{--}200 \text{ km s}^{-1}$, far below the escape velocity of the star (550 km s^{-1}).

3. Discussion

3.1. Radiation Power and Total Energy of the Flare

We tried to estimate the radiation power of the flare. We first estimated the luminosity of the continuum (L_c) under the $H\alpha$ line. Since the white-light continuum of a star generally can be approximated by the Planck function, L_c can be calculated through the following equation:

$$\begin{aligned} L_c &= 4\pi^2 R^2 \int_{6557\text{\AA}}^{6572\text{\AA}} \frac{1}{e^{hc/\lambda kT} - 1} \frac{2hc^2}{\lambda^5} d\lambda \\ &= 7.58 \times 10^{28} \text{ erg s}^{-1}, \end{aligned} \quad (5)$$

where T represents the effective temperature of the star, which is 3404.72 K . L_c represents the luminosity of the continuum between 6557 and 6572 \AA . R is the radius of the star, which is $0.411 R_\odot$.

Considering that the equivalent width of the normalized continuum in the wavelength range $6557\text{--}6572 \text{ \AA}$ is 15 \AA and the equivalent width of the $H\alpha$ line has a peak of 28.36 \AA , we can calculate the peak luminosity (L_f) of the flare through the following relation:

$$\frac{L_f}{L_c} = \frac{28.36}{15} \quad (6)$$

and L_f was estimated to be $1.43 \times 10^{29} \text{ erg s}^{-1}$.

We can also estimate the total energy of the flare from the integrated flux calculated in Section 2.2. This observation did not cover the whole process of the flare. We need to remove the $H\alpha$ contribution from non-flare state of the star. We used the average of first three spectra to estimate it, and the result in the form of equivalent width is 5.43 \AA . During the observation, from 70 minutes to 163 minutes, the flare energy radiated through $H\alpha$ is $4.45 \times 10^{32} \text{ erg}$. If we assume that the power of the flare and the equivalent width of $H\alpha$ in the last three spectra decay at the same speed as the last three spectra, we estimate that the flare lasts for 418 minutes, and the total flare energy radiated through $H\alpha$ was estimated to be $2.42 \times 10^{33} \text{ erg}$.

3.2. Mass of the Moving Plasma

We have tried to estimate the mass of the moving plasma. We decided to use the method that was first introduced by Houdebine et al. (1990) and recently used by Koller et al. (2021) to estimate the mass. We used the following formula to obtain a lower limit on the mass (Houdebine et al. 1990):

$$M \geq \frac{4\pi d^2 F_m (N_{tot}/N_j) m_H \eta_{OD}}{h\nu_{j-i} A_{j-i}} = \frac{L_m (N_{tot}/N_j) m_H \eta_{OD}}{h\nu_{j-i} A_{j-i}}, \quad (7)$$

where d is the distance from the star and F_m is the integrated excess flux of the moving plasma. Since we did not have absolute flux calibration, we used L_m , the luminosity of the moving plasma, to estimate $4\pi d^2 F_m$. N_{tot}/N_j is the ratio of the number density of hydrogen atoms and the number density of hydrogen atoms at excitation level j . m_H is the mass of a hydrogen atom. η_{OD} is the opacity damping factor. h is the Planck constant. ν_{j-i} and A_{j-i} are the frequency and Einstein coefficient of the spectral line, respectively.

As for other parameters in the formula above, we used the same settings as Koller et al. (2021) used. This flare event under study was detected from the $H\alpha$ line (transition from $j=3$ to $i=2$). However, they could not find an appropriate calculation to estimate N_{tot}/N_3 , so they decided to use the relevant data for the $H\gamma$ line ($j=5$, $i=2$) for their calculation. Houdebine et al. (1990) performed nonlocal thermal equilibrium (non-LTE) modeling for AD Leo and estimated $N_{tot}/N_5 = 2 \times 10^9$. They set η_{OD} to 2, which indicates that half of the radiation escapes the moving feature (Leitzinger et al. 2014). For $H\gamma$, A_{j-i} is 2.53×10^6 (Wiese & Fuhr 2009).

We used the same method mentioned in Section 3.1 to estimate the radiation power of the moving plasma through the red-wing enhancement of the $H\alpha$ line $L_{m,\alpha}$. In Section 2.3, we have calculated the equivalent width of the redshifted enhancement, and the equivalent width reaches a maximum

in the last exposure. The equivalent width is 3.29 \AA , which means $L_{m,\alpha}/L_c = 3.29/15$. In this way we found $L_{m,\alpha} = 1.66 \times 10^{28} \text{ erg s}^{-1}$. To obtain the radiation power of the $H\gamma$ line $L_{m,\gamma}$, we need to divide $L_{m,\alpha}$ by a factor of ~ 3 (Butler et al. 1988), just as Koller et al. (2021) did. Finally, we obtained a lower limit for the mass of the moving plasma, which is $3.2 \times 10^{15} \text{ kg}$.

3.3. Lorentz Profile of the $H\alpha$ Line

From 70 to 117 minutes, the $H\alpha$ line appears to reveal a Lorentz profile with a symmetric line broadening. Similar line broadening phenomena have been reported in observations of solar flares (e.g., Kowalski et al. 2017; Zhu et al. 2019) and also in studies of stellar flares (Fuhrmeister et al. 2018; Namekata et al. 2020), and have been interpreted as nonthermal broadening or Stark (pressure) broadening. There are two classical theories for the explanation of Stark broadening: the impact theory (Weisskopf 1932) and the statistical theory. The former results in a Lorentz profile and the latter leads to a Holtsmark profile (Holtsmark 1919). Since the observed $H\alpha$ spectra can be well fitted by a Voigt–Gauss function that includes a Lorentz profile, here we take the former to explain our current observation. According to the impact theory, each time the radiating atom collides with a charged particle, the radiation is interrupted. After a Fourier transform, this interrupted radiation forms a Lorentz profile in the frequency domain. Moreover, the RADYN numerical simulation of M-dwarf flares from Namekata et al. (2020) recently suggested that, due to the non-LTE formation properties and highly variable opacity of the $H\alpha$ line, the broadened $H\alpha$ profile observed during flares is not only determined by the Stark broadening but also sometimes relates to “opacity broadening.” Indeed, through changing the energy spectra from soft- into hard-energy input cases, their simulation results revealed that once hard high-energy electron beams appear during flares and deposit their energy in the deep chromosphere, strong self-absorptions and a Stark effect can simultaneously cause a wider line broadening. Therefore, this radiative-transfer-induced broadening process may also be important for the broadened flaring $H\alpha$ line, because stellar and solar flares are often associated with intense nonthermal radiation/heating.

Clear Lorentz profiles were observed at 70, 93, and 117 minutes, which correspond to the impulsive increase in the $H\alpha$ line intensity. On the basis of the theory mentioned above, pressure broadening implies that collisions between electrons and hydrogen atoms become more frequent, that is to say, electron density increases significantly. It is well known that in the impulsive phase of solar flares, energetic electrons are accelerated in the corona, then propagate downward along flare loops and finally collide with hydrogen atoms in the (deep) chromosphere. Meanwhile, as revealed in Namekata et al. (2020), if a strong nonthermal heating occurs in this stellar flare, the formation height of the $H\alpha$ line can further extend into the lower chromosphere and then a larger opacity (or strong self-absorption) would also contribute to a wider line broadening.

After 117 minutes, the $H\alpha$ line intensity stops increasing, indicating the end of the impulsive phase. From Figure 4 we can see that the HWHM of the Gaussian component in the Voigt–Gauss fitting function becomes nonzero again, meaning that the spectral line profiles start to deviate from a Lorentz function and the electron density begins to decrease, but the

spectral line profiles are still wider than their pre-flare state. This likely indicates that nonthermal heating, i.e., energetic electron beams, is still continuing but with a softer/weaker energy injection. Indeed, Namekata et al. (2020) recently reported a good correspondence between the white-light emission and the variation of $H\alpha$ line width in stellar flares of the M-type star AD Leo, suggesting that $H\alpha$ line broadening has a fairly good relationship with nonthermal heating. In their observed flares, a similar decrease in the $H\alpha$ line width from the impulsive to the decay phase was also found. Such a scenario is in accord with the physical explanation of the decaying phase of the flare in the standard solar flare scenario (e.g., Benz and Güdel 2010; Shibata & Magara 2011).

3.4. Redward Asymmetry of the $H\alpha$ Line Profile

On the Sun, numerous spectroscopic observations of flares have revealed that chromospheric lines often exhibit line asymmetries during flares. Redward asymmetries indicative of velocities of several tens of kilometers per second have been frequently reported during the impulsive phase of the flare. This is commonly thought to be induced by chromospheric condensation (e.g., Fisher et al. 1985), the downward movement of the chromospheric plasma caused by the high pressure in the chromosphere. Downflows of dense plasma draining back to the solar surface along post-flare loops also lead to redward asymmetries of chromospheric spectral lines (e.g., Tian et al. 2015). Blue asymmetries or blueshifts of spectral lines have also been detected in the early phase of solar flares, which indicate upflows with speeds of a few to a few hundred kilometers per second in different spectral lines. This has often been attributed to the chromospheric evaporation, namely warm/hot plasma upflows driven by intense chromospheric heating. In the meantime, CMEs may also produce absorption line asymmetries if they contain erupting filament materials. For example, Den & Kornienko (1993) reported a strong mass ejection during a solar flare through obvious blue-wing absorption in $H\alpha$, indicating a radial velocity of over 600 km s^{-1} . Similarly, Ding et al. (2003) investigated a series of filament-induced absorptions in the $H\alpha$ blue wing, revealing a good temporal correspondence between the acceleration process of a filament and the impulsive phase of a two-ribbon solar flare.

Doppler shifts or asymmetries of spectral lines have also been frequently detected during flares on other stars (e.g., Houdebine et al. 1990; Gunn et al. 1994; Crespo-Chacón et al. 2006; Vida et al. 2016; Fuhrmeister et al. 2018; Cao et al. 2019). Using X-ray observations, Argiroffi et al. (2019) recently reported a long-lasting blueshift of $\sim 90 \text{ km s}^{-1}$ of cool plasma (3 MK) in the decay phase of a large stellar flare on the evolved giant star HR 9024. They explained this cool upflow as a CME candidate. At optical wavelengths, spectral line asymmetries are more frequently reported (e.g., Leitzinger et al. 2014; Honda et al. 2018; Koller et al. 2021), although their explanations sometimes are not straightforward. For instance, Honda et al. (2018) found that the $H\alpha$ line in a stellar flare on the dMe star EV Lac exhibited a long-lived blueward asymmetry, with a velocity of $\sim 100 \text{ km s}^{-1}$, even throughout the whole duration of the flare. They speculated that the blue asymmetries might be caused by possible filament activation/eruption and evaporation, but little is yet known about the definite origin of such long-duration blue asymmetries. Koller et al. (2021) have searched for asymmetries of the Balmer lines

in time-resolved spectroscopy provided by the Sloan Digital Sky Survey data release 14 and reported six CME candidates with excess flux in line wings, with the highest projected velocities of 300–700 km s⁻¹. In fact, most (5/6) of these asymmetries appear in the red wings. Koller et al. (2021) suggested that these red-wing asymmetries may be caused by several possible processes, i.e., backward-directed CMEs occurring close to the limb, falling cool material during the eruption, or severe chromospheric condensation.

In our case, apart from obvious line broadening, red-wing asymmetries also appear during the flare process. From Figure 5, it is clear that the redward asymmetry becomes more evident after the impulsive increase in the H α intensity. This strongly suggests that such line asymmetries are a flare-induced phenomenon. The line asymmetries we detected last toward the end of our observations, when the H α intensity starts to decrease. This is timed to coincide with the line broadening after the flare peak, namely the continuing nonthermal heating. Moreover, the line asymmetries demonstrate an increasing amplitude until the end of our observations, with a redshifted velocity at 100–200 km s⁻¹. According to our current knowledge of solar flares, the long-lived red-wing enhancement may originate from three possible scenarios. (1) A flare-driven coronal rain process. The typical downward velocity of solar coronal rain is more than 100 km s⁻¹; as revealed in many observations of solar flares, coronal rain results from the radiative cooling process of hot flaring plasma that is trapped in post-flare loops, thus these loops often become more prominent in the decay phase of flares. These observed features are basically consistent with the properties of red-wing asymmetries we detected here. (2) A flare-induced chromospheric condensation process. In solar flares, chromospheric condensation results from nonthermal heating processes in flares and it usually happens in the impulsive phase, with a typical downflow velocity of tens of kilometers per second (e.g., Ding et al. 1995; Tian et al. 2015; Yu et al. 2020) but sometimes even up to or above 100 km s⁻¹ as well (e.g., Ichimoto & Kurokawa 1984; Tei et al. 2018). Here, the red-wing asymmetry is accompanied by obvious line broadening after the flare peak, thus suggesting that continuing nonthermal heating might still be responsible for the appearance of condensation downflows in the decay phase. (3) A flare-associated filament/prominence eruption either with a non-radial backward propagation or with strong magnetic suppression. In the case of a backward ejected filament, the flare must occur near or at the limb of the stellar disk, where its footpoint-produced H α emission (especially line broadening) at least can be visible from the Earth. This special requirement regarding spatial location suggests that a backward filament eruption is rare. Another situation is a failed filament eruption, which was first reported on the Sun (Ji et al. 2003) and recently supposed to be common on M-type stars due to their strong magnetic suppression (Alvarado-Gómez et al. 2018; Li et al. 2020b). In this case, the ejected filament material may be quickly confined by an overlying magnetic field after the flare peak and may then demonstrate more and more prominent downward mass falling to the stellar disk, which thus might cause the increasing amplitude of red-wing asymmetries in our observation. Meanwhile, the ejecting filament at the flare onset is expected to cause a short-lived blueshift before we detected the red-wing asymmetries. But this blueshift was absent from the LAMOST observation, possibly due to its poor temporal resolution

(around 23 mins). We caution that, by only using chromospheric spectral observations, it is very difficult to distinguish from our current observation between these three possible scenarios or their combinations, since the observed H α radiation from the star could be a superposition of flare, post-flare loop, and prominence eruption. In future, to better understand these physical processes in stellar flares, new time-resolved spectroscopic observations using multi-temperature lines are needed.

The speed of the moving plasma is 100–200 km s⁻¹, far below the star’s escape velocity. However, we should remember that this speed only represents the lower limit of the true velocity of the moving material, because the Doppler shift can only be used to measure the velocity component along the line of sight, and ejected filament material originating from the limb very likely has a small velocity component along the line of sight. Thus, we cannot exclude the possibility that a backward filament eruption might drive a CME if the red-wing asymmetries were to be an eruption. Moreover, as shown in Figure 4(e), the moving plasma responsible for the redward asymmetry likely decelerates. The average deceleration rate is computed as 7.6 m s⁻², which is much smaller than the gravity of the star. In the filament/prominence eruption scenario, this very small deceleration rate might support the idea that the ejecting filament material is flying in a nonradial direction that is nearly perpendicular to the line of sight, suffering a severe projection effect.

On the other hand, the acceleration of plasma during solar coronal rain is about $g_{\text{eff}}/3$ (Antolin 2020). If we assume that the falling materials move downward with a constant acceleration of $g_{\text{eff}}/3$ and the propagation distance scales with the radius of the star, the maximum velocity of the falling plasma on a star can be estimated as follows:

$$v = v_{\odot} \sqrt{\frac{gR}{g_{\odot}R_{\odot}}}, \quad (8)$$

where v_{\odot} is the maximum velocity of plasma during coronal rain on the Sun, which is about 100 km s⁻¹ according to Antolin (2020). g and g_{\odot} are the gravitational accelerations on the star and the Sun, respectively, and the stellar and solar radii are represented by R and R_{\odot} , respectively. Our calculation yielded a value of 126 km s⁻¹ for v , which is consistent with the velocities inferred from our RB asymmetry analysis, supporting the possible coronal rain scenario mentioned above.

4. Conclusion

From the LAMOST DR7 data archive, we identified a strong flare event on an M4-type star. The key findings are summarized as follows.

1. The flare shows an impulsive increase followed by a gradual decrease in the H α line intensity. The impulsive increase starts at 70 minutes and the H α intensity peaks at 117 minutes after the beginning of the observation. The maximum radiation power of the flare through the H α line is 1.43×10^{29} erg s⁻¹. During the observation, the flare energy radiated in H α is 4.45×10^{32} erg, and the total flare energy radiated through H α is estimated to be of the order of 10^{33} erg.
2. During the impulsive phase, the H α line appears to have a Lorentz profile, which we think is caused by downward

propagating nonthermal electrons colliding with hydrogen atoms in the chromosphere. After $t = 117$ minutes, the spectral profile gradually deviates from a Lorentz profile due to the decrease in acceleration of nonthermal electrons and the resultant decrease in electron density in the chromosphere.

3. $H\alpha$ line asymmetries corresponding to plasma moving away from the Earth at a velocity of $100\text{--}200\text{ km s}^{-1}$ are detected. The asymmetries might result from three possible scenarios: (1) flare-driven coronal rain, (2) chromospheric condensation, or (3) a filament/prominence eruption either with a nonradial backward propagation or with strong magnetic suppression. The total mass of the moving plasma is estimated to be of the order of 10^{15} kg .

H.H. is supported by the National Key R&D Program of China (grant No. 2019YFA0405000). This work is also supported by NSFC grant Nos. 11825301, 11790304, & 11973059, the fellowship of China National Postdoctoral Program for Innovative Talents (grant No. BX20200013), and Peking University Undergraduate Research Program. We thank the referee for the very helpful comments and constructive suggestions, and thank Y.-J. Zhu, Dr. Y. Li, and Dr. H. Li for helpful discussions. The Large Sky Area Multi-object Fiber Spectroscopic Telescope, LAMOST (Guoshoujing Telescope), is a National Major Scientific Project built by the Chinese Academy of Sciences. Funding for the project has been provided by the National Development and Reform Commission. LAMOST is operated and managed by the National Astronomical Observatories, Chinese Academy of Sciences.

ORCID iDs

Hechao Chen  <https://orcid.org/0000-0001-7866-4358>
 Hui Tian  <https://orcid.org/0000-0002-1369-1758>
 Jianrong Shi  <https://orcid.org/0000-0002-0349-7839>
 Han He  <https://orcid.org/0000-0001-9352-9189>
 Hongpeng Lu  <https://orcid.org/0000-0001-8037-5256>

References

- Aarnio, A. N., Stassun, K. G., Hughes, W. J., et al. 2011, *SoPh*, **268**, 195
 Alvarado-Gómez, J. D., Drake, J. J., Cohen, O., et al. 2018, *ApJ*, **862**, 93
 Alvarado-Gómez, J. D., Drake, J. J., Cohen, O., et al. 2021, arXiv:2111.09704
 Antolin, P. 2020, *PPCF*, **62**, 014016
 Argiroffo, C., Reale, F., Drake, J. J., et al. 2019, *NatAs*, **3**, 742
 Benz, A. O., & Güdel, M. 2010, *ARA&A*, **48**, 241
 Butler, C. J., Rodono, M., & Foing, B. H. 1988, *A&A*, **206**, L1
 Canfield, R. C., Penn, M. J., Wulser, J.-P., et al. 1990, *ApJ*, **363**, 318
 Cao, D., Gu, S., Ge, J., et al. 2019, *MNRAS*, **482**, 988
 Chen, H., Tian, H., Li, L., et al. 2022, *A&A*, **659**, A107
 Chen, P. F. 2011, *LRSP*, **8**, 1
 Cox, A. N., & Pilachowski, C. A. 2000, *PhT*, **53**, 77
 Crespo-Chacón, I., Montes, D., García-Alvarez, D., et al. 2006, *A&A*, **452**, 987
 Cui, X.-Q., Zhao, Y.-H., Chu, Y.-Q., et al. 2012, *RAA*, **12**, 1197
 De Pontieu, B., McIntosh, S. W., Hansteen, V. H., et al. 2009, *ApJL*, **701**, L1
 Den, O. E., & Kornienko, G. I. 1993, *ARep*, **37**, 76
 Ding, M. D., Chen, Q. R., Li, J. P., et al. 2003, *ApJ*, **598**, 683
 Ding, M. D., Fang, C., & Huang, Y. R. 1995, *SoPh*, **158**, 81
 Doyle, L., Ramsay, G., & Doyle, J. G. 2020, *MNRAS*, **494**, 3596
 Falcon, R. E., Rochau, G. A., Bailey, J. E., et al. 2015, *ApJ*, **806**, 214
 Fisher, G. H., Canfield, R. C., & McClymont, A. N. 1985, *ApJ*, **289**, 425
 Fletcher, L., Dennis, B. R., Hudson, H. S., et al. 2011, *SSRv*, **159**, 19
 Fuhrmeister, B., Czesla, S., Schmitt, J. H. M. M., et al. 2018, *A&A*, **615**, A14
 Gan, W. Q., Rieger, E., & Fang, C. 1993, *ApJ*, **416**, 886
 Ginsburg, A., & Mirocha, J. 2011, PySpecKit: Python Spectroscopic Toolkit, ascl:1109.001
 Gosling, J. T. 1993, *JGR*, **98**, 18937
 Gunn, A. G., Doyle, J. G., Mathioudakis, M., et al. 1994, *A&A*, **285**, 489
 Haisch, B., Strong, K. T., & Rodono, M. 1991, *ARA&A*, **29**, 275
 He, H., Wang, H., & Yun, D. 2015, *ApJS*, **221**, 18
 He, H., Wang, H., Zhang, M., et al. 2018, *ApJS*, **236**, 7
 Holtsmark, J. 1919, *AnP*, **363**, 577
 Honda, S., Notsu, Y., Namekata, K., et al. 2018, *PASJ*, **70**, 62
 Houdebine, E. R., Foing, B. H., & Rodono, M. 1990, *A&A*, **238**, 249
 Howell, S. B., Sobek, C., Haas, M., et al. 2014, *PASP*, **126**, 398
 Ichimoto, K., & Kurokawa, H. 1984, *SoPh*, **93**, 105
 Illing, R. M. E., & Hundhausen, A. J. 1985, *JGR*, **90**, 275
 Ji, H., Wang, H., Schmahl, E. J., et al. 2003, *ApJL*, **595**, L135
 Kanodia, S., Ramsey, L. W., Maney, M., et al. 2022, *ApJ*, **925**, 155
 Khodachenko, M. L., Ribas, I., Lammer, H., et al. 2007, *AsBio*, **7**, 167
 Koller, F., Leitzinger, M., Temmer, M., et al. 2021, *A&A*, **646**, A34
 Kowalski, A. F., Allred, J. C., Uitenbroek, H., et al. 2017, *ApJ*, **837**, 125
 Leitzinger, M., Odert, P., Greimel, R., et al. 2014, *MNRAS*, **443**, 898
 Li, D., Hong, Z., & Ning, Z. 2022, *ApJ*, **926**, 23
 Li, L., Peter, H., Chitta, L. P., et al. 2020a, *ApJ*, **905**, 26
 Li, T., Hou, Y., Yang, S., et al. 2020b, *ApJ*, **900**, 128
 Li, Y., & Ding, M. D. 2011, *ApJ*, **727**, 98
 Lin, J., Soon, W., & Baliunas, S. L. 2003, *NewAR*, **47**, 53
 Luque, J. M., Calzada, M. D., & Sáez, M. 2003, *JPhB*, **36**, 1573
 Maehara, H., Notsu, Y., Namekata, K., et al. 2021, The 20.5th Cambridge Workshop on Cool Stars, Stellar Systems, and the Sun (CS20.5), ed. S. Wolk, (Cambridge, MA: CFA), 142
 Maehara, H., Notsu, Y., Namekata, K., et al. 2021, *PASJ*, **73**, 44
 Maehara, H., Shibayama, T., Notsu, S., et al. 2012, *Natur*, **485**, 478
 Moschou, S.-P., Drake, J. J., Cohen, O., et al. 2019, *ApJ*, **877**, 105
 Muheki, P., Guenther, E. W., Mutabazi, T., et al. 2020, *A&A*, **637**, A13
 Muheki, P., Guenther, E. W., Mutabazi, T., et al. 2020, *MNRAS*, **499**, 5047
 Namekata, K., Maehara, H., Honda, S., et al. 2022, *NatAs*, **6**, 241
 Namekata, K., Maehara, H., Sasaki, R., et al. 2020, *PASJ*, **72**, 68
 Namekata, K., Sakaue, T., Watanabe, K., et al. 2017, *ApJ*, **851**, 91
 Notsu, Y., Shibayama, T., Maehara, H., et al. 2013, *ApJ*, **771**, 127
 Osten, R. A., & Wolk, S. J. 2017, in IAU Symp. 328, Living Around Active Stars, ed. D. Nandy, P. Petit, & A. Valio (Cambridge: Cambridge Univ. Press), 243
 Schad, T. A., Dima, G. I., & Anan, T. 2021, *ApJ*, **916**, 5
 Schaefer, B. E., King, J. R., & Deliyannis, C. P. 2000, *ApJ*, **529**, 1026
 Schmieder, B., Forbes, T. G., Malherbe, J. M., et al. 1987, *ApJ*, **317**, 956
 Shibata, K., Isobe, H., Hillier, A., et al. 2013, *PASJ*, **65**, 49
 Shibata, K., & Magara, T. 2011, *LRSP*, **8**, 6
 Su, D. Q., Cui, X., Wang, Y., et al. 1998, *Proc. SPIE*, **3352**, 76
 Švestka, Z. 1972, *ARA&A*, **10**, 1
 Tei, A., Sakaue, T., Okamoto, T. J., et al. 2018, *PASJ*, **70**, 100
 Tian, H., McIntosh, S. W., De Pontieu, B., et al. 2011, *ApJ*, **738**, 18
 Tian, H., McIntosh, S. W., Xia, L., et al. 2012, *ApJ*, **748**, 106
 Tian, H., Young, P. R., Reeves, K. K., et al. 2015, *ApJ*, **811**, 139
 Tremblay, P.-E., & Bergeron, P. 2009, *ApJ*, **696**, 1755
 Tu, Z.-L., Yang, M., Wang, H.-F., et al. 2021, *ApJS*, **253**, 35
 Tu, Z.-L., Yang, M., Zhang, Z. J., et al. 2020, *ApJ*, **890**, 46
 Vida, K., Kriskovics, L., Oláh, K., et al. 2016, *A&A*, **590**, A11
 Vida, K., Leitzinger, M., Kriskovics, L., et al. 2019, *A&A*, **623**, A49
 Wang, J., Xin, L. P., Li, H. L., et al. 2021, *ApJ*, **916**, 92
 Weisskopf, V. 1932, *ZPhy*, **75**, 287
 Wiese, W. L., & Fuhr, J. R. 2009, *JPCRD*, **38**, 1129
 Yan, Y., He, H., Li, C., et al. 2021, *MNRAS*, **505**, L79
 Yashiro, S., & Gopalswamy, N. 2009, in IAU Symp. 257, Universal Helio-physical Processes, ed. N. Gopalswamy et al. (Cambridge: Cambridge Univ. Press), 233
 Yelle, R., Lammer, H., & Ip, W.-H. 2008, *SSRv*, **139**, 437
 Yu, K., Li, Y., Ding, M. D., et al. 2020, *ApJ*, **896**, 154
 Zarro, D. M., Canfield, R. C., Strong, K. T., et al. 1988, *ApJ*, **324**, 582
 Zhang, M., & Low, B. C. 2005, *ARA&A*, **43**, 103
 Zhang, Q. M., Li, D., & Ning, Z. J. 2016, *ApJ*, **832**, 65
 Zhu, Y., Kowalski, A. F., Tian, H., et al. 2019, *ApJ*, **879**, 19